

Research



Cite this article: Leclercq T, Peake N, de Langre E. 2018 Does flutter prevent drag reduction by reconfiguration? *Proc. R. Soc. A* **474**: 20170678.

<http://dx.doi.org/10.1098/rspa.2017.0678>

Received: 22 September 2017

Accepted: 10 November 2017

Subject Areas:

fluid mechanics

Keywords:

drag reduction, reconfiguration, flutter, instability, fluid–structure interactions

Author for correspondence:

T. Leclercq

e-mail: tristan.leclercq@polytechnique.edu

Does flutter prevent drag reduction by reconfiguration?

T. Leclercq¹, N. Peake² and E. de Langre¹

¹Department of Mechanics, LadHyX, CNRS, École Polytechnique, 91128 Palaiseau, France

²Department of Applied Mathematics and Theoretical Physics, University of Cambridge, Wilberforce Road, Cambridge CB3 0WA, UK

TL, 0000-0002-5995-3354

The static reconfiguration of flexible beams exposed to transverse flows is classically known to reduce the drag these structures have to withstand. But the more a structure bends, the more parallel to the flow it becomes, and flexible beams in axial flows are prone to a flutter instability that is responsible for large inertial forces that drastically increase their drag. It is, therefore, unclear whether flexibility would still alleviate, or on the contrary enhance, the drag when flapping occurs on a reconfiguring structure. In this article, we perform numerical simulations based on reduced-order models to demonstrate that the additional drag induced by the flapping motion is almost never significant enough to offset the drag reduction due to reconfiguration. Isolated and brief snapping events may transiently raise the drag above that of a rigid structure in the particular case of heavy, moderately slender beams. But apart from these short peak events, the drag force remains otherwise always significantly reduced in comparison with a rigid structure.

1. Introduction

When flexible structures are placed in a fluid flow, the drag they experience is strongly modified by the deformation caused by that flow. In particular, the work of [1] has shown that plants in nature benefit from their flexibility and experience a lower drag force than if they were rigid. This ability to reduce flow-induced forces by passively adapting their shape is now thought to be a key factor in allowing aquatic organisms to survive in flow-dominated environments [2]. To better understand this phenomenon, the studies of [3,4] have analysed the mechanism of elastic reconfiguration and the resulting drag reduction of flat

plates in uniform, steady, large-Reynolds-number flow. More recent papers have additionally accounted for gravity and buoyancy [5], non-uniformities [6], non-planar deformations [7] or viscous effects [8–10].

All these studies assume static structural deflection in a steady background flow. However, the low-Reynolds-number study in [11] has shown that the vortices shed from the free tip may force a flexible fibre into a flapping motion. The efficiency of drag reduction when flapping occurs is then mitigated and depends on the mode of deformation [12]. Such self-induced dynamics has also been witnessed for large-Reynolds-number systems, for instance on tree leaves that flap in the wind [13–15]. The very occurrence of dynamics induces inertial loads that may enhance the drag, and one may wonder whether flexibility is associated with lower or larger drag in that case, compared with a rigid structure that does not reconfigure but does not flap either.

The cause and the nature of the flapping dynamics depend on the geometry of the structure and its orientation to the flow. When the structure is perpendicular to the flow, the vortices shed from the tip are obviously responsible for flow-induced vibrations [16]. Flexible structures exposed to a transverse flow become more and more aligned with it as they reconfigure, but the flapping of flags in the wind illustrates that structures parallel to the flow are also prone to self-induced dynamic oscillations [17–22]. This flag flutter instability results from the competition between the destabilizing aerodynamic pressure forces and the stabilizing rigidity of the structure, so slender structures in axial flow are also liable to it [23–28]. A few authors have tried to assess the drag of such structures theoretically [29], numerically [24] and experimentally [30–36]. All these works prove that the onset of flutter is associated with a large increase in the drag force, whose magnitude is strongly correlated to the periodicity and the envelope of the flutter mode.

As stated above, cantilever structures that bend in a transverse flow become more and more aligned with it, so that the flow about sufficiently deflected beams becomes mostly axial. If reconfiguration is known to have a drag-lowering effect that protects the structural integrity, the possible fluttering of highly reconfigured beams may, on the other hand, be responsible for a magnification of the drag, possibly leading to damage or breakage. In the literature, the small-amplitude vibrations of a naturally curved rod in a flow have been considered in [37], as well as the flapping dynamics of plates clamped in axial flow at their trailing edge instead of their leading edge (the so-called inverted flag problem [38–40]), and the flow-induced instability of filaments clamped at their trailing edge but deflected by gravity [41]. However, very little is known about the self-induced dynamics of structures passively bending under the effect of the flow, and even less about whether the resulting drag force is overall enhanced or reduced. The goal of this work is thus to determine if, and to what extent, the occurrence of flutter may impair the drag reduction abilities of flexible structures in transverse flow compared with rigid ones. We will focus on the case of cantilevered, elongated beams of arbitrary but uniform cross section.

The model used throughout the study is presented in §2. In §3, we discuss the domain of stability of the static reconfiguration. In §4, the post-critical flapping behaviour of the deflected structure is analysed. Finally, the consequences of flexibility in terms of total drag modulation when reconfiguration and flutter are both considered are discussed in §5.

2. Model

We consider the problem depicted in figure 1. A structure of length L , width W , thickness D and mass per unit length m is clamped perpendicular to a uniform and steady flow of velocity U of a fluid of density ρ .

We assume that the structure may only bend in the xz -plane and we neglect torsion or any out-of-plane deformation. The structure is elongated in the plane of bending ($L \gg D$), and we model it as a two-dimensional inextensible Euler–Bernoulli beam of bending stiffness EI [42]. The local angle θ of the tangent vector $\boldsymbol{\tau} = \boldsymbol{r}'$ is defined with respect to the vertical axis \boldsymbol{e}_z , where $\boldsymbol{r} = x(s, t)\boldsymbol{e}_x$

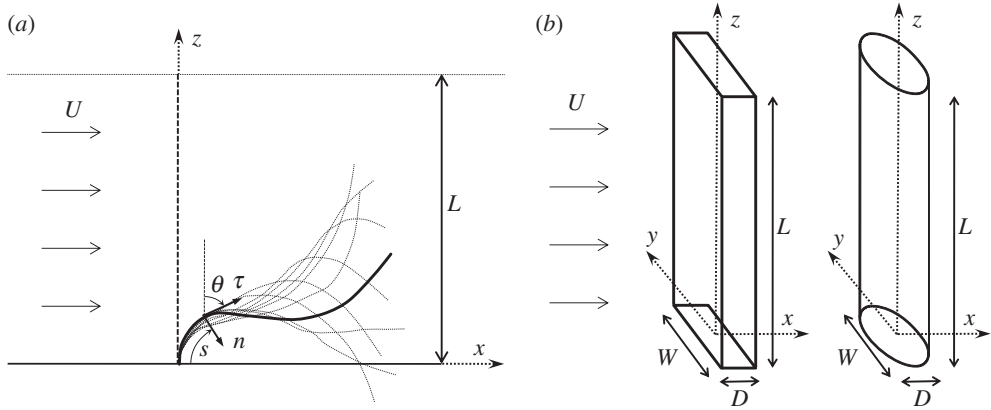


Figure 1. (a) Side view of the deforming structure. (b) Examples of geometries of two undeformed structures with different cross-section shapes.

$+z(s, t)e_z$ is the position vector and the prime symbol $(\cdot)'$ denotes differentiation with respect to the curvilinear coordinate s . Following [42], the dynamic equilibrium reads

$$m\ddot{\mathbf{r}} = \mathbf{F}' + \mathbf{q}, \quad (2.1)$$

where \mathbf{q} is the external load per unit length on the structure, $\mathbf{F} = T\boldsymbol{\tau} + Q\mathbf{n}$ is the internal force vector and the overdot stands for time derivation. The internal bending moment M is related to the local curvature $\kappa = \theta'$ by $M = EIk$, and the shear force Q is given by $Q = -M' = -EIk'$. Clamping implies $x = z = \theta = 0$ at $s = 0$, while the free tip condition reads $T = M = Q = 0$ at $s = L$.

We disregard the influence of gravity and buoyancy forces, and we restrict our study to large Reynolds number so that friction drag is neglected. More details about the influence of friction can be found in [28]. We also assume that the structure is slender ($L \gg W$) so that the flow at a given location s along the span is dominated by its local two-dimensional component in the plane of the cross section. This assumption implies that we neglect the end-wall effects so that this problem physically amounts to considering that the structure is clamped in the middle region of the flow and there is no wall. Following Eloy *et al.* [43], Singh *et al.* [44,45] or Michelin & Doaré [46], we model the effect of the flow as a combination of two external loads distributed along the span. First, the reactive (or added mass) force is related to the potential component of the flow [47,48],

$$\mathbf{q}_{\text{am}} = -m_a [\partial_t(U_n \mathbf{n}) - \partial_s(U_n U_\tau \mathbf{n}) + \frac{1}{2} \partial_s(U_n^2 \boldsymbol{\tau})], \quad (2.2)$$

where the added mass is given by $m_a = \rho\pi W^2/4$. This expression involves the normal and tangential components of the relative velocity $\mathbf{U}_r = U_\tau \boldsymbol{\tau} + U_n \mathbf{n} = \dot{\mathbf{r}} - \mathbf{U}$. In the case of an inextensible beam, this force becomes purely normal and its expression may be simplified in

$$\mathbf{q}_{\text{am}} = -m_a [\ddot{\mathbf{r}} \cdot \mathbf{n} - 2\dot{\theta} U_\tau + \kappa(U_\tau^2 - \frac{1}{2} U_n^2)] \mathbf{n}, \quad (2.3)$$

as explained in appendix A. This reactive model has been extensively used in the literature for the linear stability analysis of straight beams in axial flow [27,28,49]. Indeed, as emphasized in [44,50], it is the potential component of the flow that is driving the instability. However, when studying the large-amplitude post-critical oscillations, an additional resistive contribution \mathbf{q}_d associated with flow separation in the plane of the cross sections has proved necessary to avoid unrealistically large flapping amplitude [44]. Besides, in our case, the beam is statically deflected by the effect of the cross-flow before it starts fluttering. The reactive term \mathbf{q}_{am} vanishes on a straight and motionless beam, so the resistive contribution \mathbf{q}_d is essential to bend the beam into a configuration prone to flutter. The semi-empirical formulation of [51] is unambiguously used in

the literature as a flapping amplitude-limiting term in flutter studies such as [43–45] or [46], as well as the driving force in the static reconfiguration studies of [4,6]. It reads

$$q_d = -\frac{1}{2}\rho C_D W |U_n| U_n \mathbf{n}, \quad (2.4)$$

where C_D is a drag coefficient that depends on the geometry of the cross section and that is typically of order $O(1)$. For instance, we classically have $C_D = 1$ for a circular cross section, and $C_D = 1.8$ for a flat plate with rectangular cross section.

Combining (2.3) and (2.4) in the right-hand side of equation (2.1) yields the governing equation

$$m\ddot{\mathbf{r}} = [T + \frac{1}{2}EI\kappa^2]\boldsymbol{\tau} + [\kappa T - EI\kappa'']\mathbf{n} + \mathbf{q}_{am} + \mathbf{q}_d. \quad (2.5)$$

After projection on the tangential and normal directions and elimination of the unknown tension T , we finally obtain a single integro-differential equation on the kinematic variables $\kappa, \theta, \mathbf{r}$:

$$\begin{aligned} (m + m_a)\ddot{\mathbf{r}} \cdot \mathbf{n} - m\kappa \int_L^s \ddot{\mathbf{r}} \cdot \boldsymbol{\tau} \, ds + EI \left[\kappa'' + \frac{1}{2}\kappa^3 \right] \\ + m_a \left[\kappa \left(U_\tau^2 - \frac{1}{2}U_n^2 \right) - 2\dot{\theta}U_\tau \right] + \frac{1}{2}\rho C_D W |U_n| U_n = 0. \end{aligned} \quad (2.6)$$

Following de Langre *et al.* [28] and Païdoussis [49], we non-dimensionalize all the variables using the length of the structure L and the scale of the natural period of the structure in small-amplitude oscillations in the fluid $T_s = L^2\sqrt{(m + m_a)/EI}$. We finally obtain, in non-dimensional form,

$$\ddot{\mathbf{r}} \cdot \mathbf{n} - (1 - \beta)\kappa \int_1^s \ddot{\mathbf{r}} \cdot \boldsymbol{\tau} \, ds + \kappa'' + \frac{1}{2}\kappa^3 + \beta \left[\kappa \left(U_\tau^2 - \frac{1}{2}U_n^2 \right) - 2\dot{\theta}U_\tau \right] + \beta\lambda |U_n| U_n = 0, \quad (2.7)$$

with the inextensibility condition $\mathbf{r}' = \boldsymbol{\tau}$, the boundary conditions $\mathbf{r} = 0, \theta = 0$ at the clamped edge $s = 0$ and $\kappa = \kappa' = 0$ at the free tip $s = 1$. The non-dimensional relative velocity is given by $U_\tau \boldsymbol{\tau} + U_n \mathbf{n} = \dot{\mathbf{r}} - u/\sqrt{\beta} \mathbf{e}_x$. This system is ruled by three non-dimensional parameters that are

$$\beta = \frac{m_a}{m_a + m}, \quad u = UL\sqrt{\frac{m_a}{EI}} \quad \text{and} \quad \lambda = \frac{\rho C_D WL}{2m_a} = \left(\frac{2}{\pi} C_D \right) \frac{L}{W}. \quad (2.8)$$

The mass ratio β represents the amount of fluid inertia within the total inertia of the system. It takes values between 0 and 1. For instance, $\beta \rightarrow 0$ for a very dense structure, $\beta = 0.5$ for a neutrally buoyant cylinder with circular cross section and $\beta \rightarrow 1$ for very thin plates ($D \ll W$). The reduced velocity u compares the relative magnitude of the fluid inertial (or reactive) load with the internal elasticity forces. Both are classically used in studies about the flutter of slender beams in axial flow, as in [49] or [28], while the third parameter $\lambda = O(L/W)$ is mostly a slenderness parameter specific to the geometry of the structure. It can also be seen as the ratio of the resistive drag to the reactive force. Because our model is only valid for elongated structures, we are restricted to $\lambda \gg 1$.

As already mentioned, the flutter instability results from the competition between the destabilizing effect of the reactive force and the stabilizing effect of the rigidity of the structure. The reduced velocity u is therefore the natural parameter that governs this phenomenon. On the other hand, the static reconfiguration of the beam is primarily due to the resistive drag overcoming the bending stiffness of the structure. The classical non-dimensional parameter that compares these two forces is the Cauchy number C_Y [52–54]. In the case of a slender structure bending in transverse flow, we define the Cauchy number following [4] as $C_Y = \rho C_D W L^3 U^2 / 2EI$. These two non-dimensional parameters are redundant as they both provide scaling of the flow velocity with respect to the structural stiffness. They are related via the slenderness parameter by $C_Y = \lambda u^2$. However, the Cauchy number is more relevant to describe reconfiguration, while the reduced velocity is more relevant to discuss features of the flutter instability.

3. Stability of the static reconfiguration

To discuss the joint effect of flutter and reconfiguration, we first need to identify the domain in which flutter may happen, and that in which the structure will reconfigure without flapping. To do so, let us first look for the stationary equilibrium solutions of the governing equation (2.7). Removing all unsteady terms in equation (2.7) yields the static equation

$$\kappa'' + \frac{1}{2}\kappa^3 + \frac{C_Y}{\lambda} \left(\sin^2 \theta - \frac{1}{2} \cos^2 \theta \right) \kappa - C_Y \cos^2 \theta = 0, \quad (3.1)$$

with boundary conditions $\theta = 0$ at $s = 0$ and $\kappa = \kappa' = 0$ at $s = 1$. This equation is independent of the mass ratio β , and depends exclusively on the Cauchy number C_Y and the slenderness parameter λ . In the limit of infinite slenderness $\lambda \rightarrow +\infty$, we recover the model in [4,6] based on the equilibrium between the elastic forces and the resistive drag to describe static reconfiguration. The numerical results in [55] have proved that the static contribution of the reactive force $O(C_Y/\lambda)$ is negligible as soon as the slenderness $\lambda \gtrsim 10$ so that the results of [4,6] remain valid for slender structures, regardless of their actual aspect ratio. However, by analogy with beams in axial flow, we expect the static shape solution of equation (3.1) to become unstable to some flutter instability as the flow velocity exceeds some threshold and the structure aligns with the flow.

To determine the stability threshold, we make use of Lyapunov's indirect method as advocated in [56] and applied in [57] regarding the stability of cantilever fluid-conveying pipes with an inclined terminal nozzle. Namely, for each value of the parameters, we perform a global linear stability analysis of the dynamic governing equation (2.7) with the corresponding boundary conditions, about the stationary equilibrium solution of equation (3.1) for that particular set of parameters. Thus, we expand the instantaneous position vector and angle θ as

$$\mathbf{r}(s, t) = \mathbf{r}_0(s) + \xi(s, t) \boldsymbol{\tau}_0(s) + \eta(s, t) \mathbf{n}_0(s) \quad \text{and} \quad \theta(s, t) = \theta_0(s) + \delta\theta(s, t), \quad (3.2)$$

where the subscript '0' refers to quantities related to the stationary solution, and ξ , η and $\delta\theta$ are small-amplitude time-dependent perturbations of the same order. At the linear order, the tangential and normal vectors read

$$\boldsymbol{\tau}(s, t) = \boldsymbol{\tau}_0(s) + \delta\theta(s, t) \mathbf{n}_0(s) \quad \text{and} \quad \mathbf{n}(s, t) = \mathbf{n}_0(s) - \delta\theta(s, t) \boldsymbol{\tau}_0(s). \quad (3.3)$$

Linearization of the inextensibility condition $\mathbf{r}' = \boldsymbol{\tau}$ provides two relations between the small variables

$$\xi' - \kappa_0 \eta = 0 \quad \text{and} \quad \delta\theta = \eta' + \kappa_0 \xi. \quad (3.4)$$

Making use of the boundary condition $\xi = 0$ at $s = 0$, we may rewrite the tangential perturbation as

$$\xi = \int_0^s \kappa_0 \eta \, ds. \quad (3.5)$$

Finally, injecting the expansion (3.2) in equation (2.7) and making use of (3.3)–(3.5), we obtain the governing equation for the small-amplitude normal perturbation

$$\begin{aligned} \ddot{\eta} - (1 - \beta)\kappa_0 \int_1^s ds \int_0^s \kappa_0 \ddot{\eta} \, ds + 2u\sqrt{\beta} \left[S_0 \dot{\eta}' + \left(\frac{1}{2}\kappa_0 + \lambda \right) C_0 \dot{\eta} \right] \\ + \left(\left[u^2 \left(S_0^2 - \frac{1}{2} C_0^2 \right) + \frac{5}{2} \kappa_0^2 \right] \eta' \right)' + \eta^{(4)} + \left[\frac{3}{2} (\kappa_0^2)'' + \kappa_0^4 \right] \eta \\ + 2\lambda u^2 C_0 \left[S_0 \eta' + \frac{1}{2} C_0 \kappa_0 \eta \right] = 0, \end{aligned} \quad (3.6)$$

where the notations $C_0 = \cos \theta_0$ and $S_0 = \sin \theta_0$ have been used for brevity, and with the boundary conditions $\eta = \eta' = 0$ at $s = 0$ and $\eta'' = \eta''' = 0$ at $s = 1$. This equation is consistent with previous

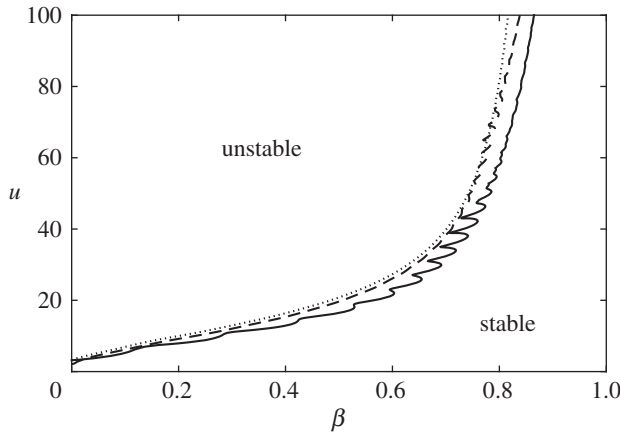


Figure 2. Critical velocity u_c as a function of the mass ratio β , for $\lambda = 10$ (solid line), $\lambda = 10^2$ (dashed line) and $\lambda = 10^3$ (dotted line).

work on slender beams in axial flow. Indeed, for $\theta_0(s) = \pi/2$ and $\kappa_0(s) = 0$ (structure parallel to the flow in the static equilibrium configuration), equation (3.6) reduces to

$$\ddot{\eta} + 2u\sqrt{\beta}\dot{\eta}' + u^2\eta'' + \eta^{(4)} = 0, \quad (3.7)$$

which is the classical small-amplitude flutter equation for an undamped beam in axial flow with no friction or gravity that is used, for instance, in [27,49] or [25].

Following [28], we then assume a perturbation of the form $\eta(s, t) = \phi(s)e^{i\omega t}$ so that equation (3.6) turns into the quadratic eigenvalue problem

$$\begin{aligned} & -\omega^2 \left[\phi - (1 - \beta)\kappa_0 \int_1^s ds \int_0^s \kappa_0 \phi ds \right] + 2iu\sqrt{\beta}\omega \left[S_0\phi' + \left(\frac{1}{2}\kappa_0 + \lambda \right) C_0\phi \right] \\ & + \phi^{(4)} + \left(\left[u^2(S_0^2 - \frac{1}{2}C_0^2) + \frac{5}{2}\kappa_0^2 \right] \phi' \right)' + 2\lambda u^2 C_0 S_0 \phi' + \left[\frac{3}{2}(\kappa_0^2)'' + \kappa_0^4 + \lambda u^2 C_0^2 \kappa_0 \right] \phi = 0, \end{aligned} \quad (3.8)$$

with the boundary conditions $\phi = \phi' = 0$ at $s = 0$ and $\phi'' = \phi''' = 0$ at $s = 1$.

To solve this numerically, the beam is discretized using $N = 100$ Gauss–Lobatto points $s_k = \frac{1}{2}(1 - \cos((k-1)/(N-1)\pi))$, and the derivatives and integrals are computed, respectively, by Chebyshev collocation and using the Clenshaw–Curtis quadrature formulae. For a given slenderness λ and mass ratio β , we first compute the static solution of equation (3.1) iteratively by increasing the Cauchy number from the upright case $C_Y = 0$. After each increment, we solve equation (3.1) with a pseudo-Newton solver (method of Broyden [58]) using the solution at the previous step as an initial guess. Then, for each value of C_Y (equivalently of u), we compute the eigenmodes $\phi(s)$ and eigenfrequencies ω by solving equation (3.8) with the Matlab function `quadeig` [59]. To check convergence of the results with respect to the mesh, computations with twice the number of points $N = 200$ were conducted and led to no significant modification of the results. For instance, the static angle at the tip of the structure $\theta_0(s=1)$ (solution of equation (3.1)) varied by less than 10^{-10} for any Cauchy number C_Y between 10^{-1} and 10^5 and for the three values of λ considered (10 , 10^2 or 10^3).

The stability thresholds are shown in figure 2 in the $\beta - u$ plane for different values of the slenderness λ . Similar to the axial case, the critical velocity increases with the mass ratio, hence making the structure heavier or the fluid lighter has a destabilizing effect. For instance, a given structure is much more likely to flap in air than in water, and neutrally buoyant structures are always stable if they are close to flat ($\beta \rightarrow 1$), while they lose stability between around $u \sim 16$ and 21 if they have a circular cross section ($\beta = 0.5$). For a given mass ratio, the critical velocity depends very little on the slenderness. Therefore, it is indeed the relative magnitude of the

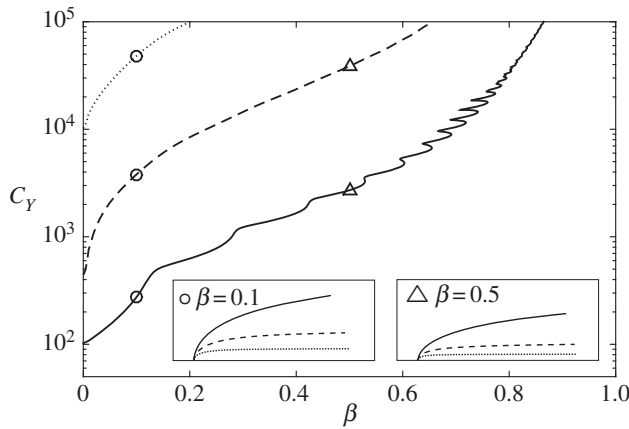


Figure 3. Critical Cauchy number $C_{Y,c}$ as a function of the mass ratio β and static equilibrium shape at the stability threshold for two specific values of the mass ratio, for $\lambda = 10$ (solid line), $\lambda = 10^2$ (dashed line) and $\lambda = 10^3$ (dotted line).

reactive fluid force and the structural stiffness that determines the onset of flutter regardless of the magnitude of the resistive drag.

On the other hand, the same stability thresholds redrawn in terms of the Cauchy number in figure 3 are obviously shifted with respect to one another as $C_Y \propto \lambda$ for a given u . Consequently, the static equilibrium shapes at the critical velocity (also shown on figure 3) are more and more deflected as slenderness is increased. Thus, we may deduce that the critical velocity does not depend on the pre-existing curvature distribution in the static equilibrium shape. More importantly, we may conclude that elongation stabilizes reconfiguration. Indeed, the more slender a structure is, the larger its critical Cauchy number $C_{Y,c}$, and so the more it may reconfigure statically before it loses stability and starts fluttering. Note finally that the critical Cauchy number is always much larger than 1. Consequently, flutter may only occur on highly reconfigured structures.

Note that, even for the most deflected cases (corresponding to $\lambda \rightarrow +\infty$) that are almost parallel to the flow, the critical velocity does not converge to that of slender beams in axial flow. This point is discussed in appendix B.

4. Post-critical kinematics

When the stability threshold is exceeded, the static solution of equation (3.1) cannot physically exist anymore. The static reconfiguration models are not valid in the unstable domain and we ought to account for the self-triggered dynamics to properly assess the drag. In this section, we start by analysing the kinematics that takes place in the post-critical regime in order to discuss its consequences in terms of drag in §5.

Hence, we now solve the full time-dependent nonlinear equation (2.7) using a time-stepping method. The time derivatives are computed using implicit second-order accurate finite differences. The time step is tuned for each case using the period T_{lin} and growth rate σ_{lin} of the most unstable eigenmode found in the linear stability analysis. It is chosen so that 100 iterations are performed over T_{lin} or $1/\sigma_{\text{lin}}$, whichever is the shortest. At $t = 0$, we combine a small contribution of the most unstable eigenmode with the static solution to initialize the system. Then, at each time step, the boundary value problem is solved with the pseudo-Newton solver used in the static case [58]. Computations are carried on a horizon such that $120 T_{\text{lin}}$ has passed, and the amplitude of the most unstable eigenmode would have had time to grow by a factor of 10^{10} in the linear framework, whichever lasts the longest.

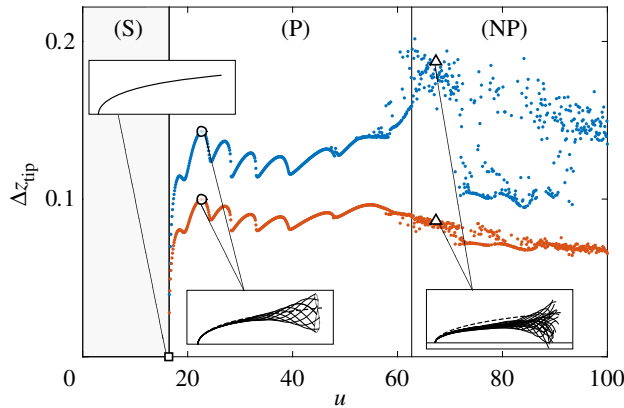


Figure 4. Vertical amplitude of flapping at the tip (blue) and standard deviation (orange) versus the reduced velocity u , for $\beta = 0.5$, $\lambda = 10$. Examples of deformation modes are shown in the thumbnails for $u = 16.4$ (square, static regime (S)), $u = 22.7$ (circle, periodic regime (P)) and $u = 67.3$ (triangle, non-periodic regime (NP)). Static equilibrium shape superimposed (dashed lines).

(a) Kinematic regimes

For the sake of clarity, let us first focus on the reference case of a neutrally buoyant circular cylinder ($\beta = 0.5$) with moderately large aspect ratio ($\lambda = 10$), before discussing the influence of varying slenderness or mass ratio in §4b. We analyse both the average and the extreme features of the dynamics, respectively, through the standard deviation and the amplitude (defined as half of the peak-to-peak amplitude measured over the simulation horizon) of the tip vertical displacement on figure 4. As is classical in flag flutter studies, three distinct regimes are identified depending on the value of u [20,21,60,61]. Each regime is illustrated in figure 4 for particular values of u in the thumbnails. Below the critical velocity $u_c = 16.5$, the structure is statically stable, so the amplitude of flapping is null. Right above the stability threshold, periodic flapping takes place. The amplitude and standard deviation both sharply increase from zero, then decrease very slowly for increasing u . The bumpy shape of these curves is most probably associated with flapping mode switches [21,61]. The amplitude is continuous at the onset of the flutter, thus indicating that the instability is supercritical. Periodic flapping is observed until $u \sim 62.7$. Above that threshold, no limit cycle can be identified in most cases and the motion is generally either quasi-periodic or chaotic. In this non-periodic regime, the standard deviation of the tip displacement remains rather continuous and of the same order of magnitude as in the periodic regime. On the other hand, the amplitude of flapping measured over the simulation horizon is rather erratic, due to the random nature of the dynamics. Overall, our results indicate that the amplitude jumps from being of the order of 0.12 to approximately 0.2. In fact, if the loss of periodicity preserves the flapping amplitude on average, it is also associated with the random occurrence of isolated, short, extreme events characterized by violent accelerations. These so-called ‘snapping events’ have also been reported in the axial configuration [20,60] and are known to be responsible for drag peaks probably at the origin of the tearing of flags [36]. Note that, owing to the random occurrence of these peaks, their magnitude may actually depend on the horizon of the simulation. Longer simulations would allow more of the most extreme events to occur and would consequently lead most probably to a larger, and smoother, amplitude. The precise features of the non-periodic dynamics such as its frequency spectrum or the probability distribution of the magnitude of the snapping events are, however, outside the scope of this article. Note also that regular flapping is still observed for some values of reduced velocity between $u \sim 72$ and $u \sim 93$, corresponding to the lower flapping amplitudes in figure 4. These occurrences are disseminated among irregular flapping cases without a clear separation, so the boundary of the periodic regime

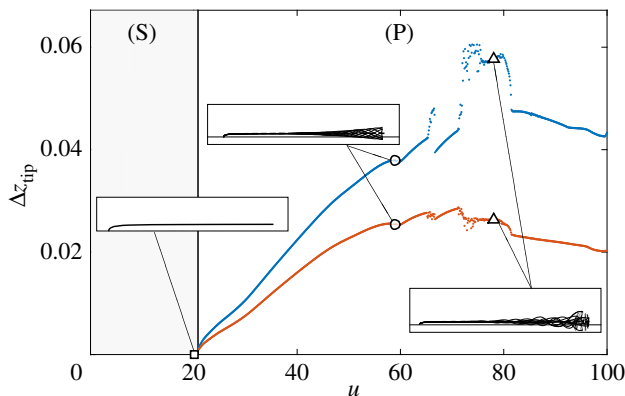


Figure 5. Vertical amplitude of flapping at the tip (blue) and standard deviation (orange) versus the reduced velocity u , for $\beta = 0.5$, $\lambda = 10^3$. Examples of deformation modes are shown in the thumbnails for $u = 20.0$ (square, static regime (S)), $u = 59.0$ (circle, periodic regime (P)) and $u = 78.0$ (triangle, periodic regime also). Static equilibrium shape superimposed (dashed lines).

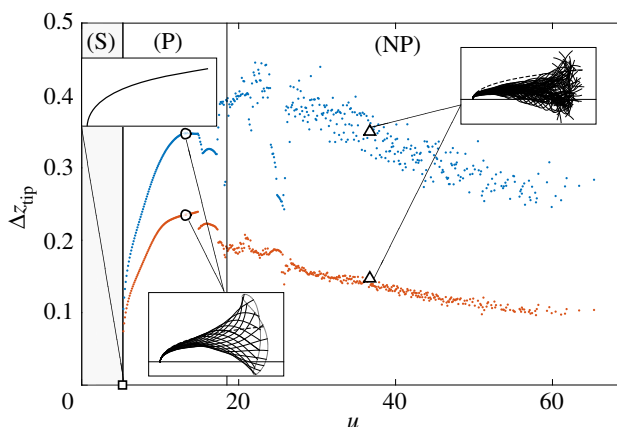


Figure 6. Vertical amplitude of flapping at the tip (blue) and standard deviation (orange) versus the reduced velocity u , for $\beta = 0.1$, $\lambda = 10$. Examples of deformation modes are shown in the thumbnails for $u = 5.2$ (square, static regime (S)), $u = 13.2$ (circle, periodic regime (P)) and $u = 36.7$ (triangle, non-periodic regime (NP)). Static equilibrium shape superimposed (dashed lines).

drawn on figure 4 is actually more of a threshold above which non-periodic motion is observed, but not exclusively.

(b) Influence of the slenderness and mass ratio

The kinematic regimes described above are affected if the slenderness or mass ratio is varied.

For instance, the same data as in figure 4 are displayed in figure 5 for a structure 100 times more elongated $\lambda = 10^3$. First, the order of magnitude of the non-dimensional amplitude of flapping is drastically decreased. Actually, it even seems that $\lambda \Delta z_{\text{tip}} = O(1)$ so that the dimensional amplitude of flapping would scale with the width of the structure, independently of its length. Similarly to the previous case, limit-cycle flapping takes place above the critical velocity $u_c = 20.8$. But, contrary to the previous case, the motion remains periodic for the whole range of reduced velocities tested. As u is increased, period multiplications and divisions successively take place, leading to more complex flapping dynamics illustrated in the thumbnail for $u = 78.0$ in figure 5. The trajectory of the tip makes several loops within a single period of the system while it simply

follows an eight-shaped trajectory in the simpler case $u = 59.0$. These flapping modes are elaborate but remain nonetheless regular and no snapping event is observed. Slenderness thus has a stabilizing effect on the nonlinear dynamics as it saturates the flapping amplitude and prevents irregular motion from taking place at large flow velocities.

The mass ratio also has an influence on the post-critical dynamics. We show in figure 6 the case of a flat plate with smaller mass ratio $\beta = 0.1$, and moderate slenderness similar to the first situation $\lambda = 10$. Similar to the reference case, periodic flapping is triggered right above the critical velocity $u_c = 5.24$ until periodicity is lost above some other threshold $u \sim 18.5$. The amplitude of flapping is, however, larger and the domain of regular flapping is reduced. Thus, reducing the mass ratio has a destabilizing effect on the nonlinear dynamics, as it enhances the flapping amplitude and favours the early transition towards irregular motion.

5. Drag reduction in the post-critical regime

The very occurrence of flutter, be it periodic or not, is known to be responsible for a significant additional drag force. Besides, its magnitude is strongly related not only to the amplitude of the flapping motion but also to its regularity as the violent accelerations associated with snapping events are responsible for enhanced drag peaks [36]. We thus expect the drag reduction abilities of the three structures introduced in §4 to be at least mitigated above the stability threshold. In this section, we discuss the modulation of drag due to flexibility for the same three structures, based on the computational results of the previous section, and in the light of the observations regarding the post-critical kinematics.

To quantify drag reduction by reconfiguration, the reconfiguration number is defined in [4] as the ratio of the drag force on the deflected structure to that on the similar but upright beam $\mathcal{R} = F/F_{\text{rigid}}$. The total drag force F is equal to the internal shear force at the base $Q(s=0) = -EI\kappa'$ ($s=0$), while the rigid drag is the integral of the resistive drag on the vertical structure of length L , $F_{\text{rigid}} = 1/2\rho C_D WLU^2$, so that the reconfiguration number reads in terms of the non-dimensional quantities $\mathcal{R} = -\kappa'(s=0)/C_Y$. When $\mathcal{R} < 1$, flexibility is responsible for lowering the drag, while it enhances it when $\mathcal{R} > 1$. Because the drag force F on the deflected structure is time dependent when flutter occurs, we will focus in the following on the time-averaged and maximum values of \mathcal{R} . The variations in the maximum and average reconfiguration numbers are related, respectively, to those of the amplitude and standard deviation of flapping.

First, figure 7 displays the variations of these two quantities with the Cauchy number C_Y in the reference case ($\beta = 0.5$, $\lambda = 10$), along with the corresponding static reconfiguration curve. The maximum and average reconfiguration numbers diverge from the static curve at the critical Cauchy number $C_{Y,c} = \lambda u_c^2 = 2.71 \times 10^3$, because of the triggering of flutter. Further increasing C_Y , the average reconfiguration number remains always larger than the static one. The self-induced dynamics is therefore responsible for an additional drag that significantly contributes to the total drag on average. However, the average reconfiguration number is decreasing with increasing C_Y so that a larger flexibility is still associated with an enhanced drag reduction above the stability threshold, on average. This trend carries on in the non-periodic as well as in the periodic regime. On the other hand, similarly to the flapping amplitude, the maximum drag sharply increases when periodicity is lost due to the occurrence of snapping events, as will be discussed in further detail later in the low mass ratio case. But, most importantly, the maximum reconfiguration number remains inferior to 1 for all values of C_Y . Therefore, no matter how large the flow velocity, the drag force remains at all times inferior to what it would be if the structure were rigid and standing upright. In other words, the additional drag due to flapping is not large enough in this case so as to completely offset the drag reduction due to reconfiguration.

This conclusion holds also for more stable structures, such as the more slender structure ($\beta = 0.5$, $\lambda = 10^3$) in §4b. In fact, we have shown in §4b that the amplitude of regular flapping is reduced compared with the reference case, so that the associated flutter-induced drag contribution is smaller. Besides, the results of §3 indicate that the instability is restricted to more deflected structures (the critical Cauchy number $C_{Y,c} = 4.33 \times 10^5$ is higher), associated

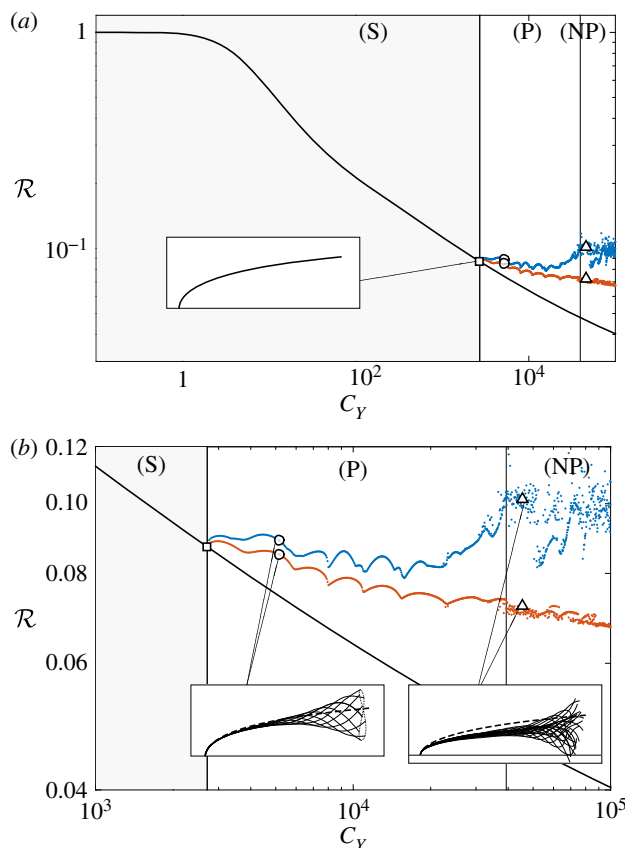


Figure 7. Reconfiguration number \mathcal{R} versus the Cauchy number C_Y , time average (orange) and maximum (blue), for $\beta = 0.5$, $\lambda = 10$. Static reconfiguration number (black). The same examples of deformation modes as in figure 4 are shown in the thumbnails, corresponding, respectively, to $C_Y = 2.69 \times 10^3$ (square, static regime (S)), $C_Y = 5.15 \times 10^3$ (circle, periodic regime (P)) and $C_Y = 4.53 \times 10^4$ (triangle, non-periodic regime (NP)). Static equilibrium shape superimposed (dashed line). (b) Simply a zoom of the lower right corner of (a).

with larger static drag. Consequently, the relative contribution of flutter-induced drag to the total drag is now almost negligible, and the reconfiguration numbers displayed in figure 8 are almost superimposed on the static curve.

The situation of a less stable structure such as the low mass ratio plate ($\beta = 0.1$, $\lambda = 10$) of §4b is actually more intricate. As for the two previous cases, the average \mathcal{R} displayed in figure 9 keeps decreasing slowly (or remains almost constant) above the stability threshold, regardless of the regularity of the flapping motion. Thus, a larger flexibility is still responsible for an alleviation (or at least no enhancement) of the drag on average even when flutter is triggered at an early stage of reconfiguration, when the amplitude of flapping is large, and in spite of the early loss of periodicity. On the other hand, the sharp increase in the flapping amplitude in the non-periodic regime may induce large enough flutter-induced drag forces so as to increase the total drag in excess of its static value. The maximum reconfiguration number increases above 1 in these cases, as, for instance, in the case $C_Y = 1.35 \times 10^4$ in figure 9. The variations of \mathcal{R} through time for this case in figure 10 confirm that this peak of drag is related to a very brief, rare, snapping event. If the peak value of the drag during one of those snapping events exceeds the largest load, the structure may endure; flexibility may in this particular case and at this particular moment be responsible for structural failure. Nonetheless, the rareness and brevity of these events make their contribution negligible on average, and flexibility remains responsible for a large overall reduction in drag, at almost any moment, in spite of flapping.

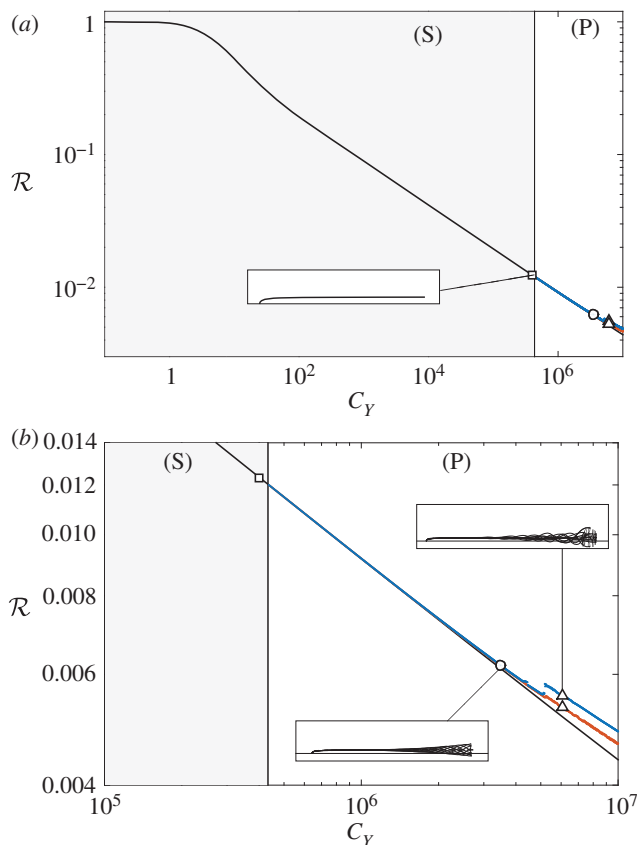


Figure 8. Reconfiguration number \mathcal{R} versus the Cauchy number C_Y , time average (orange) and maximum (blue), for $\beta = 0.5$, $\lambda = 10^3$. Static reconfiguration number (black). The same examples of deformation modes as in figure 5 are shown in the thumbnails, corresponding, respectively, to $C_Y = 4.00 \times 10^5$ (square, static regime (S)), $C_Y = 3.48 \times 10^6$ (circle, periodic regime (P)) and $C_Y = 6.08 \times 10^6$ (triangle, periodic regime also). Static equilibrium shape superimposed (dashed line). (b) Simply a zoom of the lower right corner of (a).

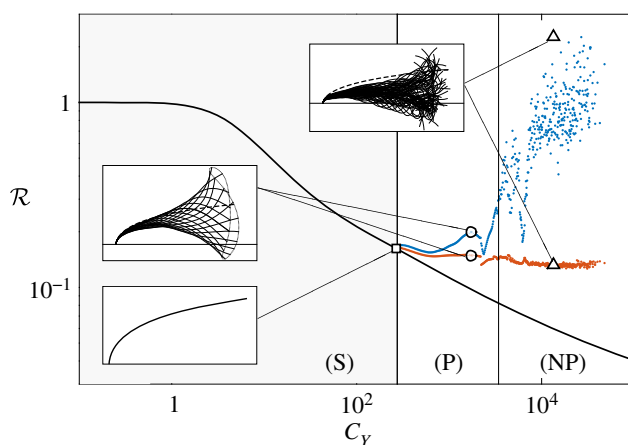


Figure 9. Reconfiguration number \mathcal{R} versus the Cauchy number C_Y , time average (orange) and maximum (blue), for $\beta = 0.1$, $\lambda = 10$. Static reconfiguration number (black). The same examples of deformation modes as in figure 6 are shown in the thumbnails, corresponding, respectively, to $C_Y = 2.70 \times 10^2$ (square, static regime (S)), $C_Y = 1.74 \times 10^3$ (circle, periodic regime (P)) and $C_Y = 1.35 \times 10^4$ (triangle, non-periodic regime (NP)). Static equilibrium shape superimposed (dashed line).

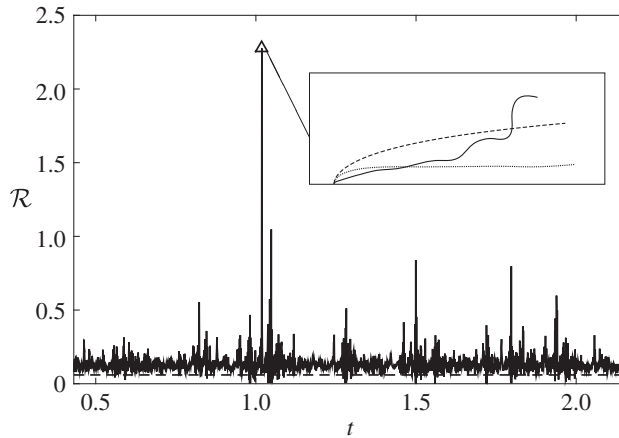


Figure 10. Time series of the reconfiguration number in the non-periodic regime of case $\beta = 0.1$, $\lambda = 10$, $C_Y = 1.35 \times 10^4$ (equivalently $u = 36.7$) corresponding to the thumbnail shown in figures 6 and 9. Level of the static reconfiguration number drawn for comparison (dashed line). The time interval displayed corresponds to the whole simulation, apart from the transient regime. Largest snapping event at $t_{\text{snap}} = 1.019$ (triangle). The shape of the structure at t_{snap} is shown in the thumbnail (solid line), along with the static shape (dashed line) and the average shape (dotted line).

6. Discussion

In this study, we have addressed the question of how flexibility may affect the drag of structures exposed to transverse flows, when the competing influences of reconfiguration and flutter are simultaneously considered. First, we performed a linear stability analysis to determine the domain in which dynamics comes into play. Then we performed nonlinear simulations in the time domain to analyse how the occurrence of dynamics alters the total drag force in the post-critical domain.

We may finally draw the following conclusions. First, it appears that, in spite of an additional flutter-induced drag contribution, the total drag of flexible structures is still reduced overall in comparison with rigid structures. Flutter may only occur when the structure reaches an advanced level of reconfiguration, so that the drag associated with the flapping motion is never large enough to fully offset the already significant reduction due to bending. Thus, flutter does not prevent drag reduction by reconfiguration.

However, the triggering of dynamics does lower the extent to which the drag of flexible structures is reduced, depending on the slenderness λ and mass ratio β of the structure. Increasing either of these parameters has a threefold stabilizing effect that tends to abate the flutter-induced contribution to drag. Firstly, both parameters are positively correlated with the stability threshold in terms of the Cauchy number $C_{Y,c}$, so the level of reconfiguration reachable before losing stability is enhanced when any of the two parameters is increased. Secondly, the amplitude of flapping is negatively correlated with β and λ , and so is the magnitude of the additional drag force. Thirdly, both parameters have a regularizing effect on the post-critical dynamics in the sense that the larger β and λ are, the larger the flow velocity may get before periodicity of the dynamics is lost. This last point is particularly important because, when flapping is irregular, very large inertial forces may transiently raise the total drag in excess of the rigid value during short snapping events. In that case, flexibility may possibly be the cause of structural damage if the failure threshold is reached. But this situation may only happen for heavy structures with moderate slenderness, and only during rare and very brief occurrences. The order of magnitude of the drag remains otherwise comparable to its mean value, which is much reduced compared with the rigid case in any situation. Therefore, we may finally conclude that the ability of flexible structures to alleviate drag by reconfiguration, albeit lessened by the flapping motion, generally prevails nonetheless in spite of flutter.

Data accessibility. This work has no additional data.

Authors' contributions. T.L., N.P. and E.d.L. conceived the project. T.L. performed the computations. All the authors contributed to the paper.

Competing interests. We declare we have no competing interests.

Funding. The authors acknowledge financial support from the DGA/DSTL grant no. 2014.60.0005.

Appendix A. Simplification of the reactive force

In the particular case of an inextensible structure, the reactive force (2.2) is purely normal and may be simplified in (2.3). Indeed, developing and sorting the terms in equation (2.2) yields

$$\mathbf{q}_{\text{am}} = -m_a[(\dot{U}_n - U'_n U_\tau - U_n U'_\tau + \frac{1}{2}\kappa U_n^2)\mathbf{n} + (U'_n + \kappa U_\tau - \dot{\theta})\boldsymbol{\tau}]. \quad (\text{A } 1)$$

Differentiating the relative velocity equation $U_\tau \boldsymbol{\tau} + U_n \mathbf{n} = \dot{\mathbf{r}} - \mathbf{U}$ with respect to s and using the inextensibility condition $\mathbf{r}' = \boldsymbol{\tau}$ provides

$$(U'_\tau - \kappa U_n)\boldsymbol{\tau} + (U'_n + \kappa U_\tau)\mathbf{n} = \dot{\mathbf{r}}' = \dot{\boldsymbol{\tau}} = \dot{\theta}\mathbf{n}, \quad (\text{A } 2)$$

so that the tangential component of equation (A 1) vanishes and $U'_\tau = \kappa U_n$ and $U'_n = \dot{\theta} - \kappa U_\tau$. Using these expressions, equation (A 1) further simplifies in

$$\mathbf{q}_{\text{am}} = -m_a[\dot{U}_n - \dot{\theta} U_\tau + \kappa(U_\tau^2 - \frac{1}{2}U_n^2)]\mathbf{n}. \quad (\text{A } 3)$$

Differentiating the relative velocity with respect to time now provides

$$(\dot{U}_\tau - \dot{\theta} U_n)\boldsymbol{\tau} + (\dot{U}_n + \dot{\theta} U_\tau)\mathbf{n} = \ddot{\mathbf{r}}, \quad (\text{A } 4)$$

so that projection on the normal vector gives $\dot{U}_n = \ddot{\mathbf{r}} \cdot \mathbf{n} - \dot{\theta} U_\tau$. Making use of that expression in equation (A 3) finally yields equation (2.3).

Appendix B. Comparison with the stability of the axial configuration

For asymptotically large slenderness $\lambda \rightarrow +\infty$, the structure aligns with the flow, and one might expect it to behave similarly to the classical axial configuration. However, figure 11 shows that the critical velocity for large slenderness does not converge to the threshold expected for an elongated beam in axial flow. In fact, even though $\theta_0 \rightarrow \pi/2$ almost everywhere, the product λC_0 remains of order $O(1)$ so that the contribution of the resistive drag remains significant even on the part of the structure that is nearly parallel to the flow. Consequently, in the limit of infinite slenderness,

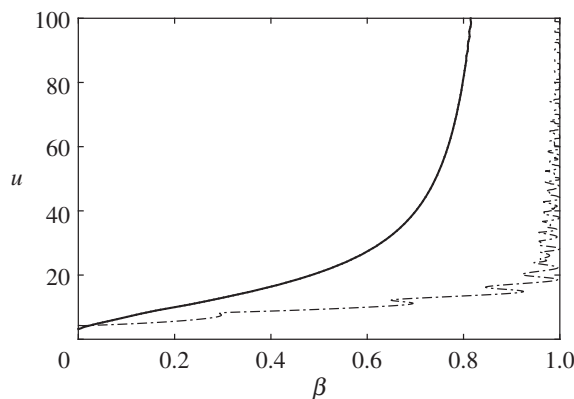


Figure 11. Linear stability thresholds obtained with the full equation (3.6) for $\lambda = 10^3$ (dotted line), with the equation relative to the axial configuration (3.7) (dashed dotted line) and with the asymptotic equation (B 1) for $\lambda = 10^3$ (solid line).

equation (3.6) actually reduces to the classical elongated small-amplitude equation in axial flow equation (3.7), but supplemented by the non-vanishing resistive drag contribution

$$\ddot{\eta} + 2u\sqrt{\beta}\dot{\eta}' + u^2\eta'' + \eta^{(4)} + 2\lambda C_0 \left(u\sqrt{\beta}\dot{\eta} + u^2\eta' \right) = 0. \quad (\text{B } 1)$$

The stability curve found for $\lambda = 10^3$ with this asymptotic equation on figure 11 is indistinguishable from that obtained with the full equation (3.6). Quite understandably, this persistent drag term introduces some additional damping that stabilizes the system compared with the axial configuration, as soon as $\beta \gtrsim 0.024$.

References

1. Vogel S. 1984 Drag and flexibility in sessile organisms. *Am. Zool.* **24**, 37–44. (doi:10.1093/icb/24.1.37)
2. Harder DL, Speck O, Hurd CL, Speck T. 2004 Reconfiguration as a prerequisite for survival in highly unstable flow-dominated habitats. *J. Plant. Growth. Regul.* **23**, 98–107. (doi:10.1007/s00344-004-0043-1)
3. Alben S, Shelley M, Zhang J. 2004 How flexibility induces streamlining in a two-dimensional flow. *Phys. Fluids* **16**, 1694–1713. (doi:10.1063/1.1668671)
4. Gosselin F, de Langre E, Machado-Almeida BA. 2010 Drag reduction of flexible plates by reconfiguration. *J. Fluid Mech.* **650**, 319–341. (doi:10.1017/S0022112009993673)
5. Luhar M, Nepf HM. 2011 Flow-induced reconfiguration of buoyant and flexible aquatic vegetation. *Limnol. Oceanogr.* **56**, 2003–2017. (doi:10.4319/lo.2011.56.6.2003)
6. Leclercq T, de Langre E. 2016 Drag reduction by elastic reconfiguration of non-uniform beams in non-uniform flows. *J. Fluids Struct.* **60**, 114–129. (doi:10.1016/j.jfluidstructs.2015.10.007)
7. Hassani M, Mureithi NW, Gosselin F. 2016 Large coupled bending and torsional deformation of an elastic rod subjected to fluid flow. *J. Fluids Struct.* **62**, 367–383. (doi:10.1016/j.jfluidstructs.2015.12.009)
8. Zhu L, Peskin CS. 2007 Drag of a flexible fiber in a 2D moving viscous fluid. *Comput. Fluids* **36**, 398–406. (doi:10.1016/j.compfluid.2006.02.002)
9. Zhu L. 2008 Scaling laws for drag of a compliant body in an incompressible viscous flow. *J. Fluid Mech.* **607**, 387–400. (doi:10.1017/S0022112008002103)
10. Alvarado J, Comtet J, de Langre E, Hosoi AE. 2017 Nonlinear flow response of soft hair beds. *Nat. Phys.* **13**, 1014–1019. (doi:10.1038/nphys4225)
11. Zhu L. 2007 Viscous flow past a flexible fibre tethered at its centre point: vortex shedding. *J. Fluid Mech.* **587**, 217–234. (doi:10.1017/S002211200700732X)
12. Yang X, Liu M, Peng S. 2014 Smoothed particle hydrodynamics and element bending group modeling of flexible fibers interacting with viscous fluids. *Phys. Rev. E* **90**, 063011. (doi:10.1103/PhysRevE.90.063011)
13. Vogel S. 1989 Drag and reconfiguration of broad leaves in high winds. *J. Exp. Bot.* **40**, 941–948. (doi:10.1093/jxb/40.8.941)
14. Miller LA, Santhanakrishnan A, Jones S, Hamlet C, Mertens K, Zhu L. 2012 Reconfiguration and the reduction of vortex-induced vibrations in broad leaves. *J. Exp. Biol.* **215**, 2716–2727. (doi:10.1242/jeb.064501)
15. Tadrist L, Julio K, Saudreau M, de Langre E. 2015 Leaf flutter by torsional galloping: experiments and model. *J. Fluids Struct.* **56**, 1–10. (doi:10.1016/j.jfluidstructs.2015.04.001)
16. Kim D, Gharib M. 2011 Flexibility effects on vortex formation of translating plates. *J. Fluid Mech.* **677**, 255–271. (doi:10.1017/jfm.2011.82)
17. Kornecki A, Dowell EH, O'Brien J. 1976 On the aeroelastic instability of two-dimensional panels in uniform incompressible flow. *J. Sound. Vib.* **47**, 163–178. (doi:10.1016/0022-460X(76)90715-X)
18. Huang L. 1995 Flutter of cantilevered plates in axial flow. *J. Fluids Struct.* **9**, 127–147. (doi:10.1006/jfls.1995.1007)
19. Watanabe Y, Suzuki S, Sugihara M, Sueoka Y. 2002 An experimental study of paper flutter. *J. Fluids Struct.* **16**, 529–542. (doi:10.1006/jfls.2001.0435)
20. Connell BSH, Yue DKP. 2007 Flapping dynamics of a flag in a uniform stream. *J. Fluid Mech.* **581**, 33–67. (doi:10.1017/S0022112007005307)

21. Michelin S, Llewellyn Smith SG, Glover BJ. 2008 Vortex shedding model of a flapping flag. *J. Fluid Mech.* **617**, 1–10. (doi:10.1017/S0022112008004321)
22. Shelley MJ, Zhang J. 2011 Flapping and bending bodies interacting with fluid flows. *Annu. Rev. Fluid Mech.* **43**, 449–465. (doi:10.1146/annurev-fluid-121108-145456)
23. Datta SK, Gottenberg WG. 1975 Instability of an elastic strip hanging in an airstream. *J. Appl. Mech.* **42**, 195–198. (doi:10.1115/1.3423515)
24. Yadykin Y, Tenetov V, Levin D. 2001 The flow-induced vibration of a flexible strip hanging vertically in a parallel flow. Part 1: temporal aeroelastic instability. *J. Fluids Struct.* **15**, 1167–1185. (doi:10.1006/jfls.2001.0400)
25. Païdoussis MP, Grinevich E, Adamovic D, Semler C. 2002 Linear and nonlinear dynamics of cantilevered cylinders in axial flow. Part 1: physical dynamics. *J. Fluids Struct.* **16**, 691–713. (doi:10.1006/jfls.2002.0447)
26. Semler C, Lopes JL, Augu N, Païdoussis MP. 2002 Linear and nonlinear dynamics of cantilevered cylinders in axial flow. Part 3: nonlinear dynamics. *J. Fluids Struct.* **16**, 739–759. (doi:10.1006/jfls.2002.0445)
27. Lemaitre C, Hémon P, de Langre E. 2005 Instability of a long ribbon hanging in axial air flow. *J. Fluids Struct.* **20**, 913–925. (doi:10.1016/j.jfluidstructs.2005.04.009)
28. de Langre E, Païdoussis MP, Doaré O, Modarres-Sadeghi Y. 2007 Flutter of long flexible cylinders in axial flow. *J. Fluid Mech.* **571**, 371–389. (doi:10.1017/S002211200600317X)
29. Moretti PM. 2003 Tension in fluttering flags. *Int. J. Acoustics Vibration* **8**, 227–230. (doi:10.20855/ijav.2003.8.4148)
30. Fairthorne RA. 1930 Drag of flags. In *Aeronautical Research Committee Reports and Memoranda*, no. 1345, pp. 887–891. London, UK: HM Stationery Office.
31. Hoerner SF. 1965 *Fluid dynamic drag*. Bricktown, NJ: SF Hoerner.
32. Taneda S. 1968 Waving motions of flags. *J. Phys. Soc. Japan* **24**, 392–401. (doi:10.1143/JPSJ.24.392)
33. Carruthers AC, Filippone A. 2005 Aerodynamic drag of streamers and flags. *J. Aircr.* **42**, 976–982. (doi:10.2514/1.9754)
34. Morris-Thomas MT, Steen S. 2009 Experiments on the stability and drag of a flexible sheet under in-plane tension in uniform flow. *J. Fluids Struct.* **25**, 815–830. (doi:10.1016/j.jfluidstructs.2009.02.003)
35. Wilk A, Skuta M. 2009 Laboratory tests of the aerodynamic drag coefficient of the flag as a body with low stiffness. *Task Quarterly* **13**, 5–14.
36. Viot E, Amandolese X, Hémon P. 2013 Fluttering flags: an experimental study of fluid forces. *J. Fluids Struct.* **43**, 385–401. (doi:10.1016/j.jfluidstructs.2013.09.012)
37. Ni Q, Li M, Tang M, Wang Y, Luo Y, Wang L. 2014 In-plane and out-of-plane free vibration and stability of a curved rod in flow. *J. Fluids Struct.* **49**, 667–686. (doi:10.1016/j.jfluidstructs.2014.06.008)
38. Gurugubelli PS, Jaiman RK. 2015 Self-induced flapping dynamics of a flexible inverted foil in a uniform flow. *J. Fluid Mech.* **781**, 657–694. (doi:10.1017/jfm.2015.515)
39. Tang C, Liu N-S, Lu X-Y. 2015 Dynamics of an inverted flexible plate in a uniform flow. *Phys. Fluids* **27**, 073601. (doi:10.1063/1.4923281)
40. Sader JE, Cossé J, Kim D, Fan B, Gharib M. 2016 Large-amplitude flapping of an inverted flag in a uniform steady flow—a vortex-induced vibration. *J. Fluid Mech.* **793**, 524–555. (doi:10.1017/jfm.2016.139)
41. Schouveiler L, Eloy C, Le Gal P. 2005 Flow-induced vibrations of high mass ratio flexible filaments freely hanging in a flow. *Phys. Fluids* **17**, 047104. (doi:10.1063/1.1878292)
42. Audoly B, Pomeau Y. 2010 *Elasticity and geometry: from hair curls to the non-linear response of shells*. Oxford, UK: Oxford University Press.
43. Eloy C, Kofman N, Schouveiler L. 2012 The origin of hysteresis in the flag instability. *J. Fluid Mech.* **691**, 583–593. (doi:10.1017/jfm.2011.494)
44. Singh K, Michelin S, de Langre E. 2012 Energy harvesting from axial fluid-elastic instabilities of a cylinder. *J. Fluids Struct.* **30**, 159–172. (doi:10.1016/j.jfluidstructs.2012.01.008)
45. Singh K, Michelin S, de Langre E. 2012 The effect of non-uniform damping on flutter in axial flow and energy-harvesting strategies. *Proc. R. Soc. A* **468**, 3620–3635. (doi:10.1098/rspa.2012.0145)
46. Michelin S, Doaré O. 2013 Energy harvesting efficiency of piezoelectric flags in axial flows. *J. Fluid Mech.* **714**, 489–504. (doi:10.1017/jfm.2012.494)

47. Lighthill MJ. 1971 Large-amplitude elongated-body theory of fish locomotion. *Proc. R. Soc. Lond. B* **179**, 125–138. (doi:10.1098/rspb.1971.0085)
48. Candelier F, Boyer F, Leroyer A. 2011 Three-dimensional extension of Lighthill's large-amplitude elongated-body theory of fish locomotion. *J. Fluid Mech.* **674**, 196–226. (doi:10.1017/S002211201000649X)
49. Païdoussis MP. 1998 *Fluid-structure interactions: slender structures and axial flow*, vol. 2. London, UK: Academic Press.
50. Eloy C, Souilliez C, Schouveiler L. 2007 Flutter of a rectangular plate. *J. Fluids. Struct.* **23**, 904–919. (doi:10.1016/j.jfluidstructs.2007.02.002)
51. Taylor GI. 1952 Analysis of the swimming of long and narrow animals. *Proc. R. Soc. Lond. A* **214**, 158–183. (doi:10.1098/rspa.1952.0159)
52. Tickner EG, Sacks AH. 1969 Engineering simulation of the viscous behavior of whole blood using suspensions of flexible particles. *Circ. Res.* **25**, 389–400. (doi:10.1161/01.RES.25.4.389)
53. Chakrabarti SK. 2002 *The theory and practice of hydrodynamics and vibration*, vol. 20. Hackensack, NJ: World Scientific.
54. de Langre E. 2008 Effects of wind on plants. *Annu. Rev. Fluid Mech.* **40**, 141–168. (doi:10.1146/annurev.fluid.40.111406.102135)
55. Leclercq T, de Langre E. In press. Reconfiguration of elastic blades in oscillatory flow. *J. Fluid Mech.*
56. Dupuis C, Rousselet J. 1992 The equations of motion of curved pipes conveying fluid. *J. Sound Vib.* **153**, 473–489. (doi:10.1016/0022-460X(92)90377-A)
57. Lundgren TS, Sethna PR, Bajaj AK. 1979 Stability boundaries for flow induced motions of tubes with an inclined terminal nozzle. *J. Sound. Vib.* **64**, 553–571. (doi:10.1016/0022-460X(79)90804-6)
58. Broyden CG. 1965 A class of methods for solving nonlinear simultaneous equations. *Math. Comput.* **19**, 577–593. (doi:10.1090/S0025-5718-1965-0198670-6)
59. Hammarling S, Munro CJ, Tisseur F. 2013 An algorithm for the complete solution of quadratic eigenvalue problems. *ACM Trans. Math. Software (TOMS)* **39**, 18. (doi:10.1145/2450153.2450156)
60. Alben S, Shelley MJ. 2008 Flapping states of a flag in an inviscid fluid: bistability and the transition to chaos. *Phys. Rev. Lett.* **100**, 074301. (doi:10.1103/PhysRevLett.100.074301)
61. Alben S. 2008 The flapping-flag instability as a nonlinear eigenvalue problem. *Phys. Fluids* **20**, 104106. (doi:10.1063/1.3000670)